Chinese Chemical Letters 36 (2025) 110344

Contents lists available at ScienceDirect

Chinese Chemical Letters

journal homepage: www.elsevier.com/locate/cclet

High-throughput screening of high energy density $LiMn_{1-x}Fe_xPO_4$ *via* active learning

Qingyun Hu[a,b], Wei Wang[c], Junyuan Lu[a], He Zhu[d], Qi Liu[c,e,*], Yang Ren[c], Hong Wang[a,b], Jian Hui[a,b,*]

[a] School of Materials Science and Engineering, Shanghai Jiao Tong University, Shanghai 200240, China
[b] Zhang Jiang Institute for Advanced Study, Shanghai Jiao Tong University, Shanghai 201210, China
[c] Department of Physics, City University of Hong Kong, Hong Kong 999077, China
[d] Herbert Gleiter Institute of Nanoscience, School of Materials Science and Engineering, Nanjing University of Science and Technology, Nanjing 210094, China
[e] Shenzhen Research Institute, City University of Hong Kong, Shenzhen 518057, China

ARTICLE INFO

Article history:
Received 18 May 2024
Revised 5 July 2024
Accepted 16 August 2024
Available online 17 August 2024

Keywords:
High-throughput screening
Machine learning
Cathode material
Performance optimization
Quantitative map

ABSTRACT

Lithium-ion batteries (LiBs) with high energy density have gained significant popularity in smart grids and portable electronics. $LiMn_{1-x}Fe_xPO_4$ (LMFP) is considered a leading candidate for the cathode, with the potential to combine the low cost of $LiFePO_4$ (LFP) with the high theoretical energy density of $LiMnPO_4$ (LMP). However, quantitative investigation of the intricate coupling between the Fe/Mn ratio and the resulting energy density is challenging due to the parametric complexity. It is crucial to develop a universal approach for the rapid construction of multi-parameter mapping. In this work, we propose an active learning-guided high-throughput workflow for quantitatively predicting the Fe/Mn ratio and the energy density mapping of LMFP. An optimal composition ($LiMn_{0.66}Fe_{0.34}PO_4$) was effectively screened from 81 cathode materials *via* only 5 samples. Model-guided electrochemical analysis revealed a non-linear relationship between the Fe/Mn ratio and electrochemical properties, including ion mobility and impedance, elucidating the quantitative chemical composition-energy density map of LMFP. The results demonstrated the efficacy of the method in high-throughput screening of LiBs cathode materials.

Lithium-ion batteries (LIBs) have emerged as one of the focal points in the field of energy storage, playing a critical role in a wide range of applications from portable electronic devices to electric vehicles [1,2]. Raising the energy density of LIBs has become increasingly important because of the higher performance required by electric vehicles for both long cruising ranges and faster charging speeds [3,4]. Currently, the energy density of LIBs is limited by cathode materials [5]. Among them, the olivine-type $LiMn_{1-x}Fe_xPO_4$ (LMFP) is considered one of the most promising cathode materials for advanced LIBs due to the potential to combine the superior safety coupled with the low-cost characteristics of $LiFePO_4$ (LFP) [6,7] and high theoretical energy density (701 mWh/g) of $LiMnPO_4$ (LMP) [8].

It is well known that the Fe/Mn ratio is a critical factor that influences the energy density of LMFP [9,10]. Recently, efforts have been devoted to exploring the correlation between the Fe/Mn ratio and energy density [10-13]. However, due to the intricate relationships of synthesis-composition-structure-property, screening the optimal Fe/Mn ratio for $LiMn_{1-x}Fe_xPO_4$ remains challenging. In addition, the mechanisms of the effects of the Fe/Mn ratio on the performance require comprehensive investigation. The traditional methodologies for optimization are mostly based on trial-and-error approaches, which are costly, laborious, and time-consuming. Consequently, a systematic and efficient investigation of the coupling relationship between the Fe/Mn ratio and the energy density becomes imperative for the design of LMFP.

Nowadays, machine learning (ML) has been widely utilized to optimize multiple parameters and establish quantitative synthesis-composition-structure-property maps [14-16]. With adequate training data, ML models could accelerate the discovery and design of materials. However, limited experimental data poses a formidable challenge for directly coupling ML with cathode materials experiments [17,18]. Recently, active learning-driven research has been successfully employed in the optimization process of functional materials [19,20]. The approach offers a viable solution by strategically designing subsequent high-valued experiments for model iterative improvement, achieving high predictive accuracy with a minimal dataset.

* Corresponding authors.
E-mail addresses: qiliu63@cityu.edu.hk (Q. Liu), hj20151107@sjtu.edu.cn (J. Hui).

https://doi.org/10.1016/j.cclet.2024.110344
1001-8417/

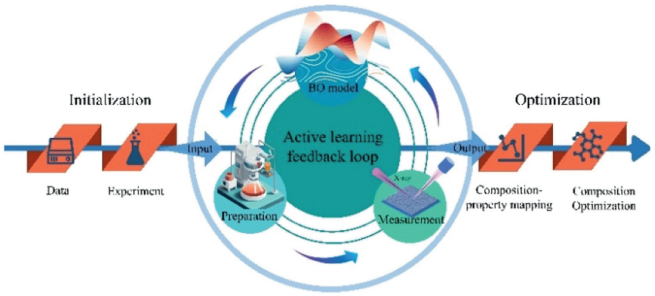

Fig. 1. A schematic of the high-throughput "Experiment-Predict-Experiment" closed-loop feedback workflow.

In this work, we propose a high-throughput materials optimization approach for the Fe/Mn ratio optimization based on a small set of experimental data, driven by active learning. The Fe/Mn ratio has been rapidly optimized ($LiMn_{0.66}Fe_{0.34}PO_4$) from 81 cathode materials *via* only 5 samples. We demonstrate that $LiMn_{0.66}Fe_{0.34}PO_4$ also exhibits remarkable rate performance and structural stability. Additionally, the electrochemical analyses with the assistance of the prediction model offer insights into the nonlinear relationship between ion mobility and impedance with the Fe/Mn ratio. The model is also used to construct the quantitative composition-energy density map of LMFP. This optimization method is proven efficient and robust in designing cathode with limited data.

The high-throughput active learning workflow – an "experiment-prediction-experiment" feedback loop for Fe/Mn ratio optimization is depicted in Fig. 1. A Bayesian optimization (BO) model has been built and continuously updated based on experiment data strategically designed by the acquisition function until it meets predefined termination criteria. The detailed construction procedures of the workflow are described as follows:

(1) Initialization: An original BO model is trained based on an initial training set, which contains an evenly selected set of points to maximize the information entropy.
(2) Experiment design: To balance exploration and exploitation, the upper confidence bound (UCB) acquisition function [21] is employed to select candidate compositions for the next synthesis. This function enables the selection of materials with the highest predicted energy density while accounting for expected uncertainties in less accurate regions of the search space. This sampling strategy aims to accelerate progress toward the specified objective while considering expected uncertainties, which enhances the accuracy and robustness of the BO model.
(3) Model Update: Subsequent synthesis experiments are conducted, electrochemical characterization results are acquired, and the BO model is updated as the measured data is fed into the training set.
(4) Termination Criteria: The iteration continues until the uncertainty falls below a predefined threshold value or the same candidate is selected consecutively. Finally, the optimal Fe/Mn ratio is determined.

The BO model we used was derived from sklearn.gaussian_process package [22]. The UCB acquisition function, which serves to guide the selection of candidate materials for synthesis, is defined as follows:

$$UCB(X) = Y(X) + 1500 \cdot Std \quad (1)$$

Here, X is the Fe content in LMFP, Y(X) is the predicted energy density that depends on the Fe/Mn ratio, and Std is the standard deviation of the BO model. The Fe/Mn ratio corresponding to the maximum value of the UCB will be selected as the next experimental target.

It has been demonstrated that excessive levels of Fe or Mn have a detrimental impact on energy density [9,12]. In this study, the range of x value, representing the content of Fe in LMFP, was optimized between [0.1, 0.9], encompassing 81 candidate compositions with a precision of 1%. To maximize information entropy, samples of four compositions, namely $LiMn_{0.8}Fe_{0.2}PO_4$, $LiMn_{0.6}Fe_{0.4}PO_4$, $LiMn_{0.4}Fe_{0.6}PO_4$, and $LiMn_{0.2}Fe_{0.8}PO_4$, were first synthesized and characterized to form the initial training datasets. The X-ray diffraction (XRD) patterns of those compositions are depicted in Fig. 2a, which indicates that all the samples are in olivine-type structures. Refinements are then performed using the GSAS II software [23] for $LiMn_{1-x}Fe_xPO_4$ in the Pmnb space group, as illustrated in Fig. 2b. The fitted cell parameters in Fig. 2c are directly proportional to x, indicating that the samples are perfect solid solution materials and are advantageous for investigating the coupling effect of Mn and Fe. As illustrated in Fig. 2d, the samples exhibit an ellipsoidal morphology with an approximate diameter of 500 nm. This suggests that the lithium diffusion paths are relatively short in the samples, which are conducive to capacity release and the optimization of specific energy.

The four cathode samples are assembled into half-cells and subjected to electrochemical testing. The specific energies of $LiMn_{1-x}Fe_xPO_4$ ($x = 0.2$, 0.4, 0.6, and 0.8) are measured and employed to train the initial BO model. Fig. 3a displays the prediction outcomes of the preliminary model with a predicted curve aligned with the experimental data and the selected candidate $LiMn_{0.66}Fe_{0.34}PO_4$. Subsequently, the candidate is synthesized and tested, and its energy density is incorporated into the BO model. Fig. 3b depicts the predictions of the updated model and the candidate that would be explored in the next iteration. Upon the successful incorporation of the new data, the model meets the established termination criteria, signifying the end of the iterative process. As a result, an optimal Fe/Mn ratio ($LiMn_{0.66}Fe_{0.34}PO_4$) is identified after a single iteration with an energy density of 583.8 mWh/g. During the process, only five variants of $LiMn_{1-x}Fe_xPO_4$ were synthesized and characterized, demonstrating the high efficiency of the model in guiding experimental efforts.

The green area in Figs. 3a and b represents the confidence interval, with a narrower shadowed area indicating a more robust model and better coherence [24]. A significant reduction in the shaded area is observed post-iteration, and the mean standard deviation of the BO model is reduced to 16.6% of the original, confirming the effectiveness of the framework in establishing the correlation between the Fe/Mn ratio and energy density. To further validate the precision of the model in identifying the Fe/Mn ratio for LMFP with the highest energy density, additional samples of $LiMn_{0.65}Fe_{0.35}PO_4$ and $LiMn_{0.67}Fe_{0.33}PO_4$ are prepared and characterized. The measured energy densities for these samples are 579.4 mWh/g and 577.8 mWh/g, respectively, which are both lower than that of $LiMn_{0.66}Fe_{0.34}PO_4$. Although discrepancies exist between the experimental energy densities of $LiMn_{0.65}Fe_{0.35}PO_4$ and $LiMn_{0.67}Fe_{0.33}PO_4$ and predicted values (580.3 mWh/g and 580.1 mWh/g), the experimental results fall within the 99.9% confidence interval.

The electrochemical performance of LMFP/C is measured to investigate the effect of the Fe/Mn ratio in LMFP materials on their electrochemical properties. Fig. 4a depicts the discharge profiles of LMFP/C. As the Fe/Mn ratio is reduced, the 4 V voltage platform of the discharge curve expands, although the rate of expansion is slower with higher Mn content. Fig. 4b illustrates the differential capacity curves of LMFP/C at 0.1 C. As the Mn content increases, the redox potentials for redox peaks, which correspond to the Mn^{3+}/Mn^{2+} and Fe^{3+}/Fe^{2+} redox couples, exhibit

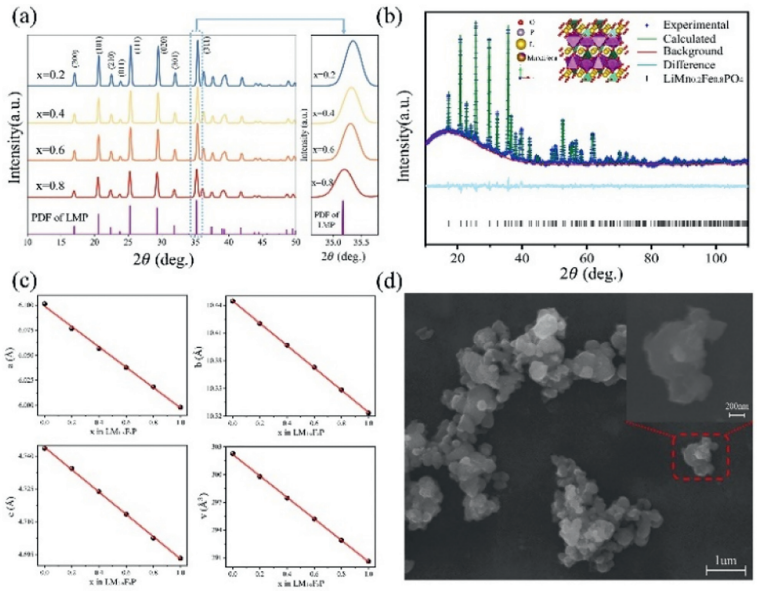

Fig. 2. Structure and morphology analysis of LMFP: (a) XRD patterns; (b) Structure refinements based on GSAS II; (c) Fitting results of cell parameters; (d) Scanning electron microscopy (SEM) image of synthesized samples.

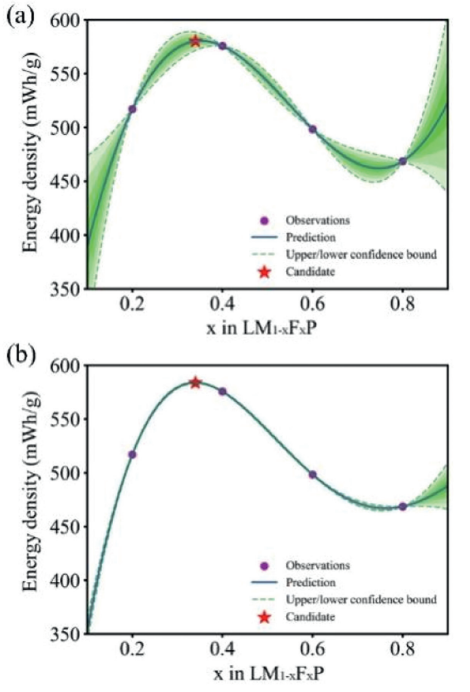

Fig. 3. Prediction curves with different confidence intervals (in green, with the lighter green indicating the higher confidence level) using BO model: (a) Original BO prediction model; (b) Updated BO prediction model after the first iteration.

a progressive increase. This upward potential shift is attributed to the enhancement of transition metals' ionic character and the reduction of the Fe 3d–O 2p antibonding state under a higher Mn content [25]. Fig. 4c presents the rate performance of LMFP during discharge at each C rate. The reversible specific capacities of $LiMn_{0.66}Fe_{0.34}PO_4$/C nanoparticles are 148.1, 137.9, 133.7, 127.3, 123.1, 115.6, 110.3, 105.4, and 99.8 mAh/g at the rates of 0.1, 0.5, 1, 3, 5, 10, 15, 20 and 25 C, respectively. The sample's capacity for recovery is observed to be satisfactory when the current density is returned to a low rate following cycling at high rates. This suggests that $LiMn_{0.66}Fe_{0.34}PO_4$ exhibits favorable structural stability

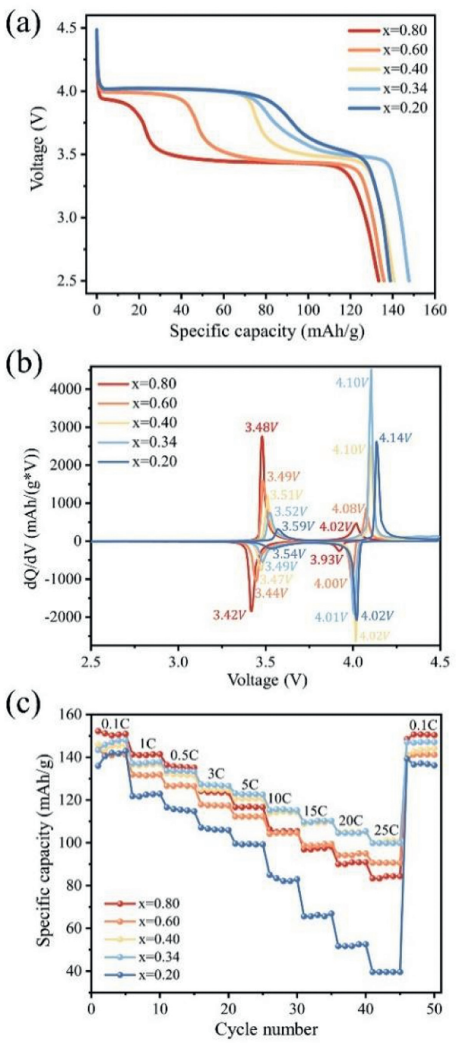

Fig. 4. Electrochemical performance of $LiMn_{1-x}Fe_xPO_4$/C electrodes. (a) Discharge curves at 0.1 C rate. (b) Differential capacity curves (d*Q*/d*V*) curves at 0.1 C rate. (c) Rate performance during discharge at each C-rate.

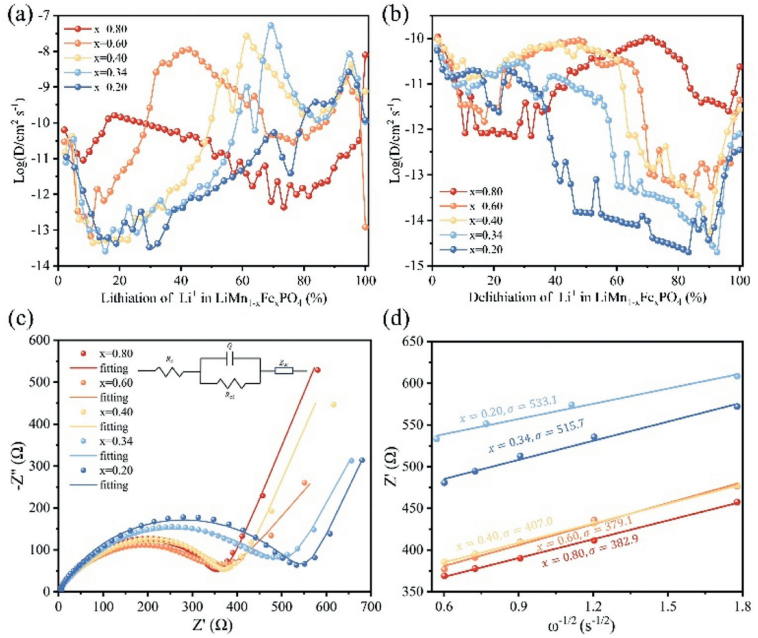

Fig. 5. Lithium diffusion coefficient trend *vs. x* (exchanged lithium ion within LMFP): (a) Lithiation; (b) Delithiation.

when cycling at a high current density. Given that the energy density of $LiMn_{0.66}Fe_{0.34}PO_4$ at 0.1 C exceeds the theoretical value of LFP (578 mWh/g) [26], this material is a promising candidate for further investigation.

The Fe/Mn ratio-energy density mapping curve derived from the BO model exhibits two distinct inflection points at $x = 0.34$ and $x = 0.75$, as shown in Fig. 3. In the intervals $0.1 \leq x \leq 0.34$ and $0.75 \leq x \leq 0.9$, a discernible rise in energy density is observed with an increment in x. Conversely, within the intermediate range of $0.34 \leq x \leq 0.75$, an inverse trend is observed, with energy density decreasing as x increases. To gain further insight into these trends, the electrochemical impedance spectroscopy (EIS) and galvanostatic intermittent titration technique (GITT) characterizations were conducted, and the results are presented in Fig. 5. The data reveal that an elevated Fe content typically reduces charge transfer resistance, thereby facilitating the diffusion of lithium ions within the LMFP/C lattice. This results in an improvement in the material's electrochemical performance. However, the impedance reduction varies across different Fe/Mn ratios due to the intricate interplay between material composition and electrochemical behavior. For instance, a decrement in x from 0.6 to 0.4 results in a slight reduction in ionic mobility and a minimal increase in impedance. In contrast, a pronounced decline in ionic mobility is observed when the x decreases from 0.4 to 0.2, accompanied by a notable increase in impedance. The nonlinearity of changes in impedance and ionic mobility can be attributed to lattice mismatches and structure transition behaviors that vary with different Fe/Mn ratios [27]. In particular, when $0.4 \leq x \leq 0.6$, the alteration in lattice mismatch [28] and the extent of the single-phase region of Fe^{3+}/Fe^{2+} and Mn^{3+}/Mn^{2+} reactions [29] is relatively minimal.

The variations in impedance and ionic mobility are the primary drivers for the changes in capacity, which in turn affect the energy density. Nevertheless, it is imperative to consider both the release of capacity and the average voltage when assessing energy density, as it is the product of these two parameters. The redox potential of Mn^{3+}/Mn^{2+} (4.1 V *vs.* Li/Li^+) is higher than that of Fe^{3+}/Fe^{2+} (3.4 V *vs.* Li/Li^+) [30], leading to a decrease in average voltage with x. On the other hand, the Jahn-Teller distortion induced by Mn^{3+} impedes Li^+ diffusion and reduces the electron conductivity, thereby reducing the attainment of the desired specific capacity [27]. Therefore, the specific capacity generally augments with an increase in x. In the ranges of $0.1 \leq x \leq 0.34$ and $0.75 \leq x \leq 0.9$, the increment in x is inadequate to offset the decline in specific capacity due to changes in ion mobility and impedance, resulting in a reduction of energy density. Within $0.34 \leq x \leq 0.75$, although average voltage increases with x, the specific capacity remains relatively stable due to minimal ion mobility and impedance changes. Thus, the Jahn–Teller effect of Mn^{3+} predominantly dictates the energy density fluctuations within $0.1 \leq x \leq 0.34$ and $0.75 \leq x \leq 0.9$, whereas the higher redox potential of Mn^{3+}/Mn^{2+} exerts the principal influence on energy density variations within the range of $0.34 \leq x \leq 0.75$.

In conclusion, we propose a strategy to optimize the Fe/Mn ratio of LMFP guided by active learning. The optimized composition ($LiMn_{0.66}Fe_{0.34}PO_4$) with the highest energy density (583.8 mWh/g) has been efficiently screened out from 81 cathode materials *via* only one iteration and five samples. The remarkable accuracy of our results was demonstrated through experimental validation. Notably, the optimal cathode exhibits favorable rate performance and structural stability. A BO model was employed to elucidate the nonlinear relationship between the Fe/Mn ratio of LMFP and its energy density, with the results being complemented by EIS and GITT measurements. This approach can be applied to optimize synthesis parameters and compounds of cathodes, thereby addressing challenges associated with limited data availability.

Declaration of competing interest

The authors declare that they have no known competing financial interests or personal relationships that could have appeared to influence the work reported in this paper.

CRediT authorship contribution statement

Qingyun Hu: Writing – original draft, Software, Methodology, Investigation, Formal analysis, Data curation, Conceptualization. **Wei Wang:** Visualization, Validation, Software, Data curation. **Junyuan Lu:** Writing – review & editing. **He Zhu:** Writing – re-

view & editing. **Qi Liu:** Writing – review & editing, Supervision. **Yang Ren:** Supervision. **Hong Wang:** Writing – review & editing, Supervision, Resources. **Jian Hui:** Writing – review & editing, Supervision.

Acknowledgments

This work was supported by the National Key Research and Development Program of China (No. 2021YFB3702102). The authors also appreciate the support from the "Initiation Program for New Teachers" (No. AF0500207), Shanghai Jiao Tong University. Qi Liu would like to acknowledge the support from the Changsha Science and Technology Plan International and Regional Cooperation Project (No. kh2304002).

Supplementary materials

Supplementary material associated with this article can be found, in the online version, at doi:10.1016/j.cclet.2024.110344.

References

[1] B. Xu, D. Qian, Z. Wang, Y.S. Meng, Mater. Sci. Engin. R: Rep. 73 (2012) 51–65.
[2] M. Tamaru, S.C. Chung, D. Shimizu, S.I. Nishimura, A. Yamada, Chem. Mater. 25 (2013) 2538–2543.
[3] Y. Tang, Y. Zhang, W. Li, B. Ma, X. Chen, Chem. Soc. Rev. 44 (2015) 5926–5940.
[4] L. Yang, W. Deng, W. Xu, et al., J. Mater. Chem. A 9 (2021) 14214–14232.
[5] K. Kang, Y.S. Meng, J. Breger, C.P. Grey, G. Ceder, Science 311 (2006) 977–980.
[6] P. Zuo, L. Wang, W. Zhang, et al., Nanoscale 7 (2015) 11509–11514.
[7] D. Choi, J. Xiao, Y.J. Choi, et al., Energy Environ. Sci. 4 (2011) 4560–4566.
[8] B. Kang, G. Ceder, Nature 458 (2009) 190–193.
[9] P.F. Xiao, B. Ding, M.O. Lai, L. Lu, J. Electrochem. Soc. 160 (2013) A918–A926.
[10] H. Yang, C. Fu, Y. Sun, L. Wang, T. Liu, Carbon 158 (2020) 102–109.
[11] J. Li, C. Guo, Y. Qin, X. Ning, Mater. Technol. 35 (2020) 565–571.
[12] J. Hong, F. Wang, X. Wang, J. Graetz, J. Power Sources 196 (2011) 3659–3663.
[13] S. Oukahou, A. Elomrani, M. Maymoun, K. Sbiaai, A. Hasnaoui, Comp. Mater. Sci. 202 (2022) 111006.
[14] Z. Wei, Q. He, Y. Zhao, J. Power Sources 549 (2022) 232125.
[15] M. Berecibar, Nature 568 (2019) 325–326.
[16] Z. Jiang, J. Li, Y. Yang, et al., Nat. Commun. 11 (2020) 2310.
[17] L. Himanen, A. Geurts, A.S. Foster, P. Rinke, Adv. Sci. 6 (2019) 1900808.
[18] J. Schmidt, M.R.G. Marques, S. Botti, M.A.L. Marques, npj Comp. Mater. 5 (2019) 83.
[19] M. Zhong, K. Tran, Y. Min, et al., Nature 581 (2020) 178–183.
[20] A.G. Kusne, H. Yu, C. Wu, H. Zhang, et al., Nat. Commun. 11 (2020) 5966.
[21] J. Winz, S. Engell, Optimization based sampling for gray-box modeling using a modified upper confidence bound acquisition function, in: 31st European Symposium on Computer Aided Process Engineering, 2021, pp. 953–958.
[22] F. Pedregosa, G. Varoquaux, A. Gramfort, et al., J. Machine Learning Res. 12 (2011) 2825–2830.
[23] B.H. Toby, R.B. Von Dreele, J. Appl. Crystal. 46 (2013) 544–549.
[24] S. Greenhill, S. Rana, S. Gupta, P. Vellanki, S. Venkatesh, IEEE Access 8 (2020) 13937–13948.
[25] G. Kobayashi, A. Yamada, S.I. Nishimura, et al., J. Power Sources 189 (2009) 397–401.
[26] S.P. Chen, D. Lv, J. Chen, Y.H. Zhang, F.N. Shi, Energy Fuels 36 (2022) 1232–1251.
[27] S. Li, H. Zhang, Y. Liu, L. Wang, X. He, Adv. Funct. Mater. 34 (2024) 2310057.
[28] A. Yamada, Y. Kudo, K.Y. Liu, J. Electrochem. Soc. 148 (2001) A1153.
[29] D.B. Ravnsbæk, K. Xiang, W. Xing, et al., Nano Lett. 16 (2016) 2375–2380.
[30] S. Wi, J. Park, S. Lee, et al., Nano Energy 31 (2017) 495–503.